Topographic Effects on the Tropical Land and Sea Breeze

TINGTING QIAN

State Key Laboratory of Severe Weather, Chinese Academy of Meteorological Sciences, Beijing, China

CRAIG C. EPIFANIO

Department of Atmospheric Sciences, Texas A&M University, College Station, Texas

FUQING ZHANG

Department of Meteorology, The Pennsylvania State University, University Park, Pennsylvania

(Manuscript received 22 December 2010, in final form 15 June 2011)

ABSTRACT

The effect of an inland plateau on the tropical sea breeze is considered in terms of idealized numerical experiments, with a particular emphasis on offshore effects. The sea breeze is modeled as the response to an oscillating interior heat source over land. The parameter space for the calculations is defined by a nondimensional wind speed, a scaled plateau height, and the nondimensional heating amplitude.

The experiments show that the inland plateau tends to significantly strengthen the land-breeze part of the circulation, as compared to the case without terrain. The strengthening of the land breeze is tied to blocking of the sea-breeze density current during the warm phase of the cycle. The blocked sea breeze produces a pool of relatively cold, stagnant air at the base of the plateau, which in turn produces a stronger land-breeze density current the following morning. Experiments show that the strength of the land breeze increases with the terrain height, at least for moderate values of the height. For very large terrain, the sea breeze is apparently blocked entirely, and further increases in terrain height lead to only small changes in land-breeze intensity and propagation.

Details of the dynamics are described in terms of the transition from linear to nonlinear heating amplitudes, as well as for cases with and without background winds. The results show that for the present experiments, significant offshore effects are tied to nonlinear frontal propagation, as opposed to quasi-linear wave features.

1. Introduction

Broadly speaking, the sea-breeze circulation consists of the local- and regional-scale responses to differential surface heating between the land and sea. This circulation plays a role in many atmospheric and oceanic phenomena in coastal areas, including thunderstorm initiation, the modulation of air pollution and fog, and the driving of wind-forced ocean currents. As such, the sea breeze has been studied extensively from a number of perspectives, including observational (Fisher 1960; Davis et al. 1889; Finkele et al. 1995; Miller et al. 2003; Puygrenier et al. 2005), numerical (Pearce 1955; Pearce et al. 1956; Estoque 1961; Fisher 1961; Antonelli and Rotunno 2007; Fovell 2005; Zhang et al. 2005), analytical (Jeffreys 1922; Haurwitz 1947; Schmidt 1947; Pierson 1950; Defant 1951, 658–672; Walsh 1974; Drobinski and Dubos 2009), and laboratory studies (Simpson 1997; Cenedese et al. 2000; Hara et al. 2009). Recent reviews are given by Miller et al. (2003) and Crosman and Horel (2010).

Most of the aforementioned studies have focused on local aspects of the sea breeze, since these local phenomena have the greatest impact on coastal populations. However, a number of recent studies have also considered the sea breeze from a mesoscale wave perspective, particularly in relation to near-shore convection in the tropics. As shown by Imaoka and Spencer (2000), Yang and Slingo (2001), Mapes et al. (2003a,b), and others, convection over the tropical oceans shows a distinct diurnal signal near coastlines, with systems initiating over land during the evening hours and then propagating

Corresponding author address: Tingting Qian, State Key Laboratory of Severe Weather, Chinese Academy of Meteorological Sciences, Beijing100081, China.
E-mail: qiantingting@cams.cma.gov.cn

DOI: 10.1175/JAS-D-11-011.1

offshore throughout the late evening and early morning. Yang and Slingo (2001) and Mapes et al. (2003b) have suggested that this propagating convective signal is likely associated with a mesoscale wave response, as produced by the diurnal heating over land. Similar suggestions have been made for propagating signals over the continents, particularly near prominent mountain ranges (Zhang and Koch 2000; Koch et al. 2001; Carbone et al. 2002; He and Zhang 2010).

The mesoscale wave dynamics of the sea breeze has been considered by only a handful of studies, mostly in the context of linear theory (Dalu and Pielke 1989; Rotunno 1983, hereafter R83). To keep the problem tractable, these studies have been cast in terms of highly idealized models, including resting background states and simple static stability profiles. The results show that for the tropics, the linear response consists of propagating internal gravity waves, while for latitudes greater than 30° the response is trapped to the coastline. An extension of the theory to include background winds was carried out recently by Qian et al. (2010, hereafter QEZ10). However, other aspects of the linear problem have received relatively little attention, including the effects of basic-state shear, static stability variations, and near-coastal terrain. The connection between the linear theory and the fully nonlinear phenomena of the sea breeze has also remained uncertain.

The goal of the present study is to explore the effect of an inland mountain range on the mesoscale aspects of the sea-breeze response, including both linear and nonlinear model calculations. As seen in the results of Imaoka and Spencer (2000) and Yang and Slingo (2001), the regions with strongest near-coastal diurnal signals are often associated with significant inland topography. In the present study, this topography is taken to be a plateau, with length scales modeled loosely on the western Columbia case considered by Mapes et al. (2003a,b) and Warner et al. (2003). The effects of the plateau are considered sequentially, beginning with the simple linear theory of QEZ10, as modified to include the topography. Nonlinear effects are then considered through experiments in which the heating amplitude and plateau height are both varied. All experiments are carried out both with and without background winds.

As in previous wave theory studies, the sea breeze is modeled as the response to a diurnally oscillating heat source. This simplification means that the study has intermediate complexity, having ties to both the simple linear wave problems, as well as the more complicated, nonlinear phenomena found in the real world. To reduce the parameter space and keep the model experiments tractable, the study is also limited to nonrotating flows (i.e., the equatorial problem).

Details of the physical setup are described in the following section. Section 3 considers the effects of topography in the linear context, focusing on both small heating amplitudes and small topography. The transition to nonlinear dynamics and intermediate topography is considered in section 4, while section 5 considers the nonlinear dynamics for large mountain heights. The final section gives a summary and discussion.

2. Model description and scaling

a. Basic physics

We consider the 2D nonrotating, compressible Boussinesq problem for a coastal mountainous region. The basic equations are given by

$$\frac{D\mathbf{u}}{Dt} = -\nabla P + b\hat{\mathbf{k}}, \tag{1}$$

$$\frac{Db}{Dt} + N^2 w = Q, \tag{2}$$

$$\frac{DP}{Dt} + c_s^2 \nabla \cdot \mathbf{u} = 0, \tag{3}$$

with

$$w = u\frac{\partial h}{\partial x} \quad \text{at} \quad z = h(x), \tag{4}$$

where $\mathbf{u} = (u_1, u_3) = (u, w)$ is the fluid velocity, P is the Boussinesq disturbance pressure, b is the buoyancy, and c_s is the Boussinesq sound speed. The background Brunt–Väisälä frequency N is taken to be constant. The function Q is a diabatic oscillating heat source, which mimics the turbulent fluxes and radiative effects over land.

The terrain shape is set to be a plateau with relatively steep sides, with length scales modeled roughly on the northern extension of the Andes. The shape of the topography is described by the smooth 2D plateau profile

$$h(x') = \begin{cases} h_0, & \text{for} \quad |x'| < L_p, \\ \dfrac{h_0}{16}\left\langle 1 + \cos\left[\dfrac{\pi(|x'|) - Lp}{4L_s}\right]\right\rangle^4, & \text{for} \quad L_p \le |x'| \le L_p + 4L_s, \\ 0, & \text{otherwise,} \end{cases} \tag{5}$$

TABLE 1. Scaling factors based on the linear theories of R83 and QEZ10.

Variable	x	z	t	u	w	b	P
Scaling factor	NH/ω	H	$1/\omega$	$Q_0/N\omega$	Q_0/N^2	Q_0/ω	Q_0H/ω

where $2L_p$ is the full width of the flat part of the plateau and L_s is roughly the half-width of the slope of the plateau. Here we set the two slopes to be symmetric. The variable x' in (5) is defined to be the distance as measured from the center of the plateau. The coastline is at $x = 0$, and the distance between the coastline and the point where $h(x)$ first reaches its maximum height is defined to be L_c. The center of the plateau is then at $x = L_c + L_p$.

The diabatic oscillating heat source is defined by

$$Q(x, z, t) = \frac{Q_0}{\pi}\left(\frac{\pi}{2} + \tan^{-1}\frac{x}{L}\right)\exp\left(-\frac{z-h}{H}\right)\cos(\omega t), \tag{6}$$

where $2L$ is roughly the half-width of the heating gradient, H is the heating depth, and ω is the diurnal frequency. Different from the heating profile used in R83 and QEZ10, this definition of the heat source includes the elevated heating gradient associated with the topography. As mentioned above, the center of the coastal zone is taken to be $x = 0$.

The scalings for this study are based on the linear theory for the sea breeze over flat terrain, as described by R83 and QEZ10. In the linear case, the depth scale is set by the H, while the depth-to-width aspect ratio as determined by the gravity wave dispersion relation is $\delta = \omega/N$. Together these two scales determine a length scale of $H/\delta = NH/\omega$. Scales for the remaining variables are then as listed in Table 1. Further discussion of these scales can be found in QEZ10.

Using the scales from Table 1 in (1)–(3) yields five nondimensional control parameters, while the terrain definition [(5)] adds four additional parameters. Together, these nine parameters completely determine the disturbance parameter space. Descriptions for the parameters are as listed in Table 2. In the present study, only three of the nine parameters will be varied: the heating amplitude ϵ, the plateau height $\mathcal{H}$, and the wind speed $\mathcal{U}$. The remaining parameters are held fixed with $\mathcal{L} = 0.091$, $\delta = 0.0073$, $\mathcal{L}_s = 0.14$, $\mathcal{L}_p = 1.36$, $\mathcal{L}_c = 0.82$, and Ma = 0.027. Values for the associated dimensional parameters are as listed below.

Figure 1 illustrates the geometry of the model problem for the sea breeze with (Fig. 1c) and without (Fig. 1a) the plateau, as well as a control case in which the heating distribution extends to infinity in both directions (Fig. 1b).

b. Model details

The simulations are calculated using the nonhydrostatic, compressible Boussinesq model described in Epifanio and Qian (2008). Acoustic propagation is handled using the time-splitting method of Klemp and Wilhelmson (1978). Terrain is included using the terrain-following coordinate of Gal-Chen and Somerville (1975). The model includes a Smagorinsky-type eddy viscosity, based loosely on the formulation of Lilly (1962). A weak background viscosity is also applied, with Reynolds number of $\mathrm{Re} = U^3 \times (\kappa N^2 L)^{-1} = 225$. The lower boundary conditions are free-slip and thermally insulating, as implemented for finite-slope topography by Epifanio (2007).

The calculations are computed in a 2D domain with horizontal extent $300L$ (or $20L_p$) and depth $18.75H$. Damping layers are imposed for the outer $48L$ of the domain in x and the upper $8.75H$ in z, with a radiation condition applied at the upper boundary. The horizontal grid spacing is $\Delta x = 0.2L$. The vertical grid spacing is $\Delta z = 0.05H$ at the ground, with vertical stretching factor of 1.005. Such small vertical grid spacing is needed to fully resolve the narrow disturbance ray paths for $U = 0$,

TABLE 2. Nondimensional control parameters for the linear wave scaling shown in Table 1.

Control parameter	Description
$\mathcal{U} = U \times (NH)^{-1}$	Background wind speed over the phase speed of the dominant linear mode
$\epsilon = Q_0 \times (N^2\omega H)^{-1}$	Stratification change due to the heating over the background stratification
$\delta = \omega/N$	Depth-to-width aspect ratio
$\mathcal{L} = \omega L \times (NH)^{-1}$	Width of the heating gradient over the width of the linear response
$\mathrm{Ma} = NH/c_s$	Phase speed of the dominant linear mode over the sound speed
$\mathcal{H} = h_0/H$	Ratio of the plateau height to the heating depth
$\mathcal{L}_s = \omega L_s \times (NH)^{-1}$	Half-width of the terrain slope over the width of the dominant linear response
$\mathcal{L}_p = \omega L_p \times (NH)^{-1}$	Plateau half-width over the width of the linear response
$\mathcal{L}_c = \omega L_c \times (NH)^{-1}$	Coast-to-plateau separation distance over the width of the linear response

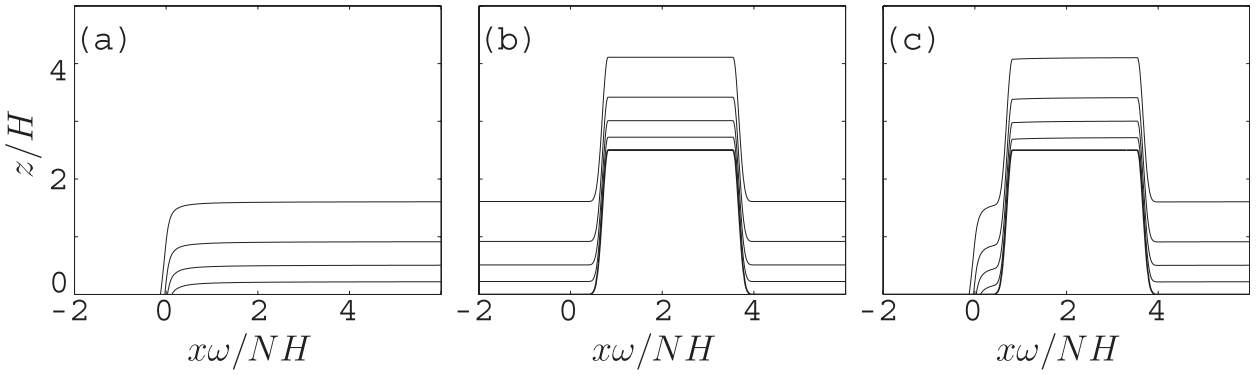

FIG. 1. The diabatic heat source [contour interval (c.i.) = 0.2] for (a) the sea-breeze case with no terrain, (b) the case of a plateau with no coastal zone, and (c) the sea-breeze case with the plateau included. The plateau height is $\mathcal{H} = 2.5$, which is the largest height considered in this study.

and to resolve the flow near the ground for $U \neq 0$. In dimensional terms, $L = 10$ km, $H = 800$ m, $N = 0.01$ s^{-1}, $\Delta x = 2$ km, and $\Delta z = 40$ m at the ground. The terrain parameters are given by $L_s = 15$ km, $L_p = 150$ km, and $L_c = 90$ km.

c. Linear calculations

In addition to the nonlinear calculations, the model described above can also be run using linearized dynamics. The model can be linearized about any arbitrary background state, as described further in section 3. The model can also be run in hydrostatic mode, which is useful when comparing to analytic calculations.

The linear model was verified for the case of flat terrain (i.e., $\mathcal{H} = 0$) by comparing to the linear analytic solution of QEZ10, which is valid for hydrostatic flow. Figures 2a and 2b show the vertical velocity for the case $\mathcal{U} = 0$ and $\mathcal{L} = 0.1$, and Figs. 2d and 2e for the case

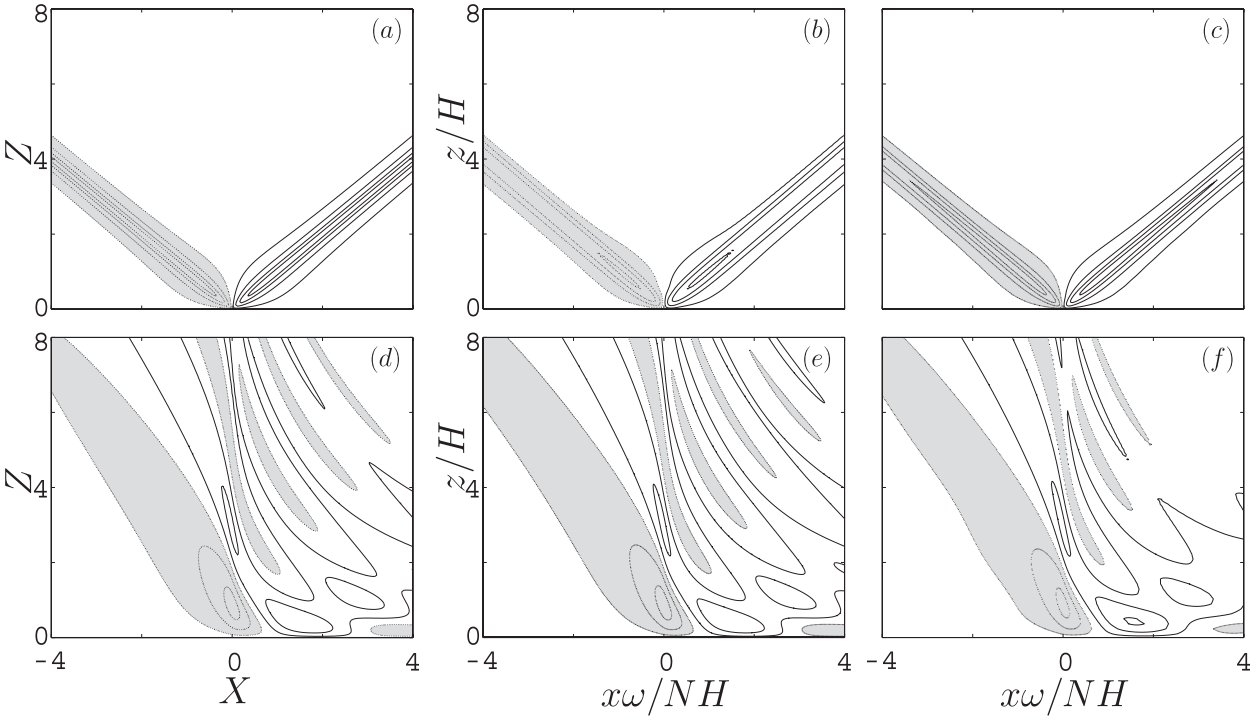

FIG. 2. Comparison of the nonviscous vertical velocity (c.i. = 0.08) with background wind (a)–(c) $\mathcal{U} = 0$ and (d)–(f) $\mathcal{U} = 0.625$ at cycle time $\omega t = \pi/2$. Shown are (a),(d) the analytical calculation results (X is the nondimensional horizontal direction, Z is the nondimensional vertical direction), (b),(e) the linear numerical results, and (c),(f) the nonlinear numerical model results.

$\mathcal{U} = 0.625$, at a time when the linear model has achieved a steady oscillation. Comparison for other values of $\mathcal{U}$ produced similar degrees of accuracy.

3. Linear wave response with small terrain

In this section, the wave disturbance produced by the heat source [(6)] is explored in the context of linearized dynamics. The computations include both background winds and coastal topography and thus form a bridge between the simple $\mathcal{H} = 0$ theory of QEZ10 and the fully nonlinear calculations of sections 4 and 5.

a. Linear calculations

The problem of flow past coastal terrain has two potential wave sources: (i) the background flow past the topography and (ii) the heating gradients due to the coastline and the terrain. Here our interest is mainly the second source. To isolate this source, we let the background state be a steady mountain wave over the plateau (as computed through a nonlinear model run) and then consider the linear disturbance produced when the heat source [(6)] is added.

To define notation, we divide the background mountain wave into two parts: a constant upstream state with wind speed U and static stability N, and the nonlinear mountain-wave disturbance denoted by u_0, w_0, b_0, and P_0. The linear disturbance produced by the heat source is then denoted by u', w', etc., so that the total wind in the x direction (for example) is $u = U + u_0 + u'$. Linearizing the 2D compressible Boussinesq system about the steady mountain wave then gives the disturbance system

$$\frac{\partial u'}{\partial t} + U\frac{\partial u'}{\partial x} + u_0\frac{\partial u'}{\partial x} + w_0\frac{\partial u'}{\partial z} + u'\frac{\partial u_0}{\partial x} + w'\frac{\partial u_0}{\partial z} = -\frac{\partial P'}{\partial x}, \tag{7}$$

$$\frac{\partial w'}{\partial t} + U\frac{\partial w'}{\partial x} + u_0\frac{\partial w'}{\partial x} + w_0\frac{\partial w'}{\partial z} + u'\frac{\partial w_0}{\partial x} + w'\frac{\partial w_0}{\partial z} = -\frac{\partial P'}{\partial x} + b', \tag{8}$$

$$\frac{\partial b'}{\partial t} + U\frac{\partial b'}{\partial x} + u_0\frac{\partial b'}{\partial x} + w_0\frac{\partial b'}{\partial z} + u'\frac{\partial b_0}{\partial x} + w'\frac{\partial b_0}{\partial z} + N^2 w' = Q, \tag{9}$$

$$\frac{\partial P'}{\partial t} + c_s^2\left(\frac{\partial u'}{\partial x} + \frac{\partial w'}{\partial z}\right) = 0, \tag{10}$$

with

$$w' = u'\frac{\partial h}{\partial x} \quad \text{at} \quad z = h(x), \tag{11}$$

where the background state is assumed known.

With the terrain added, the linear problem can no longer be addressed analytically because of the nonconstant coefficients in (7)–(11). To overcome this problem, the solutions are computed using the linearized model described in section 2c. The computation methodology involves two steps. First, using the nonlinear model, a simulation is computed without the heat source until a steady-state mountain wave is achieved over the plateau. A second simulation is then computed in which the model is linearized about the steady state from the first model run. The oscillating heat source is added and the linear model solves (7)–(11) until a steady oscillation is achieved.

For $\mathcal{H} = 0$, the linearized problem matches the sea-breeze case studied by QEZ10 (see the verification in Fig. 2). However, the terrain adds three new effects to the problem: (i) new heating gradients are produced over the terrain slopes due to the modified heating definition in (6); (ii) the disturbance flows over the sloping boundary in (11), which effectively acts as a secondary wave source; and (iii) the disturbance interacts with the background mountain wave, as shown by the extra advection terms in (7)–(9). In general these three effects are interconnected. However, as shown in the appendix, for small mountain heights the effects can be cleanly separated, with each effect appearing as a separate terrain-related wave source at leading order in h_0.

Following R83 and QEZ10, we refer to the $\mathcal{H} = 0$ solution for (7)–(11) as the linear sea-breeze wave solution. Departures from the sea-breeze case are then due to topographic effects.

b. Resting background state

For $\mathcal{U} = 0$ the background mountain wave is also zero. Only two of the mountain effects described above are then active: the elevated heating gradients and the disturbance sea-breeze flow past the topography slopes.

Figures 3a–c show the linear wave response for the case $\mathcal{U} = 0$ and for topography heights $\mathcal{H} = 0.0625$, $\mathcal{H} = 0.125$, and $\mathcal{H} = 0.625$. At small topography height the disturbances are dominated by the sea-breeze solution seen in Figs. 2a,b, but there are also small additional disturbances excited over the plateau slopes (Figs. 3a,b). The amplitude of this additional disturbance increases with topography height. When the topography height is $\mathcal{H} = 0.625$, the additional disturbance becomes the same order as the sea-breeze wave disturbance (Fig. 3c).

Figures 3d–f show the solution for the same mountain heights but with no coastline—that is, with the heat source [(6)] replaced by

$$Q(x, z, t) = Q_0 \exp\left(-\frac{z - h}{H}\right)\cos(\omega t)$$

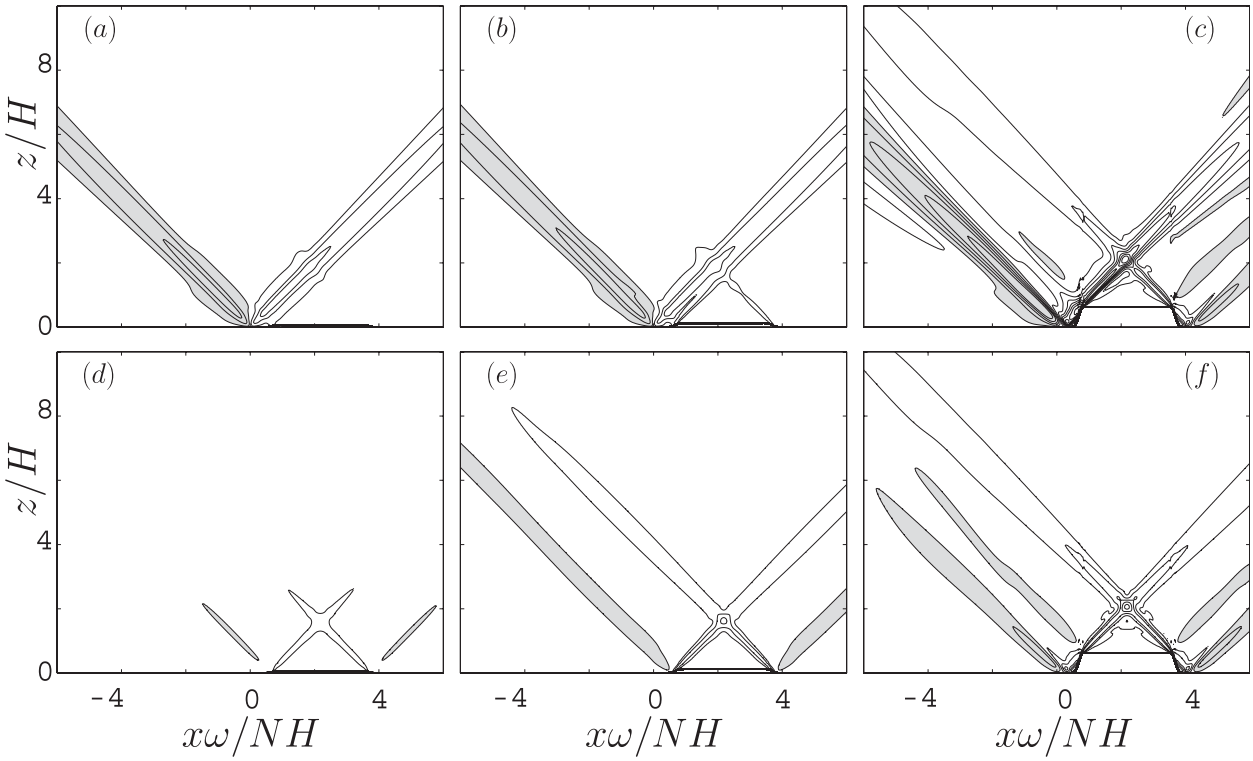

FIG. 3. Linear vertical velocity response to the diurnal heating (a)–(c) with the coastline and (d)–(f) without the coastline at $\omega t = \pi/2$ [c.i. = 0.1 in (a)–(c) and (f); c.i. = 0.04 in (d) and (e)]; $\mathcal{H}$ is set at (a),(d) 0.0625, (b),(e) 0.125, and (c),(f) 0.625.

so that heating extends everywhere along the boundary as shown in Fig. 1b. With no coastline, the sea breeze disappears and the only wave source is then the elevated heating gradients over the terrain. Figures 3d–f show that the elevated heating gradients produce disturbances over both slopes, with the amplitude of the disturbance similar to the terrain effects seen in Figs. 3a–c (note the change in contour interval). This suggests that the elevated heating source is the dominant terrain effect for $\mathcal{U} = 0$. Interestingly, comparing Figs. 3e and 3f also suggests a secondary wave source near the top of the terrain slopes when the mountain is large. These secondary waves are apparently due to the primary disturbance interacting with the steeper topography.

Note that the maximum w disturbance occurs where the disturbance ray paths intersect over the plateau. At

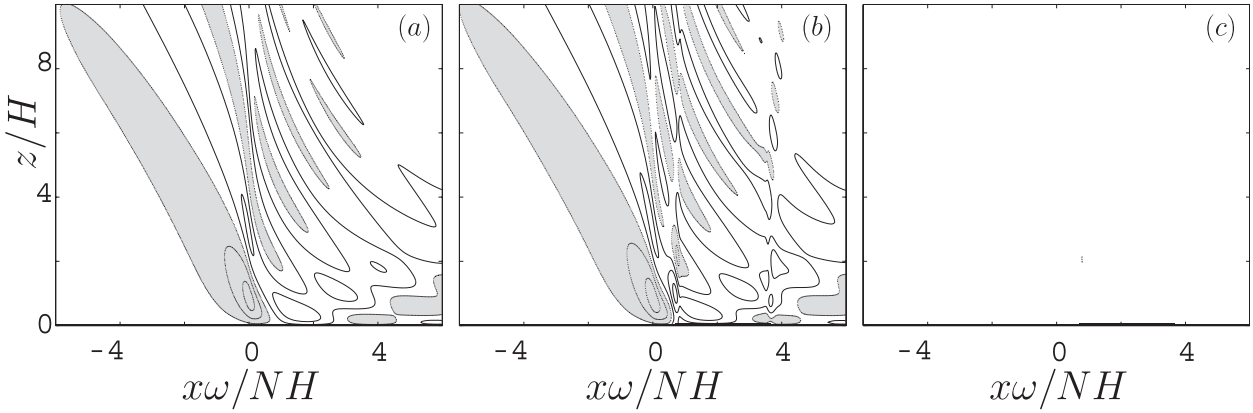

FIG. 4. Linear disturbance with $\mathcal{U} = 0.625$ at $\omega t = \pi/2$.Vertical velocity (c.i. = 0.08) in the case with (a) no terrain, (b) $\mathcal{H} = 0.031$ and coastline included, and (c) $\mathcal{H} = 0.031$ and coastline excluded.

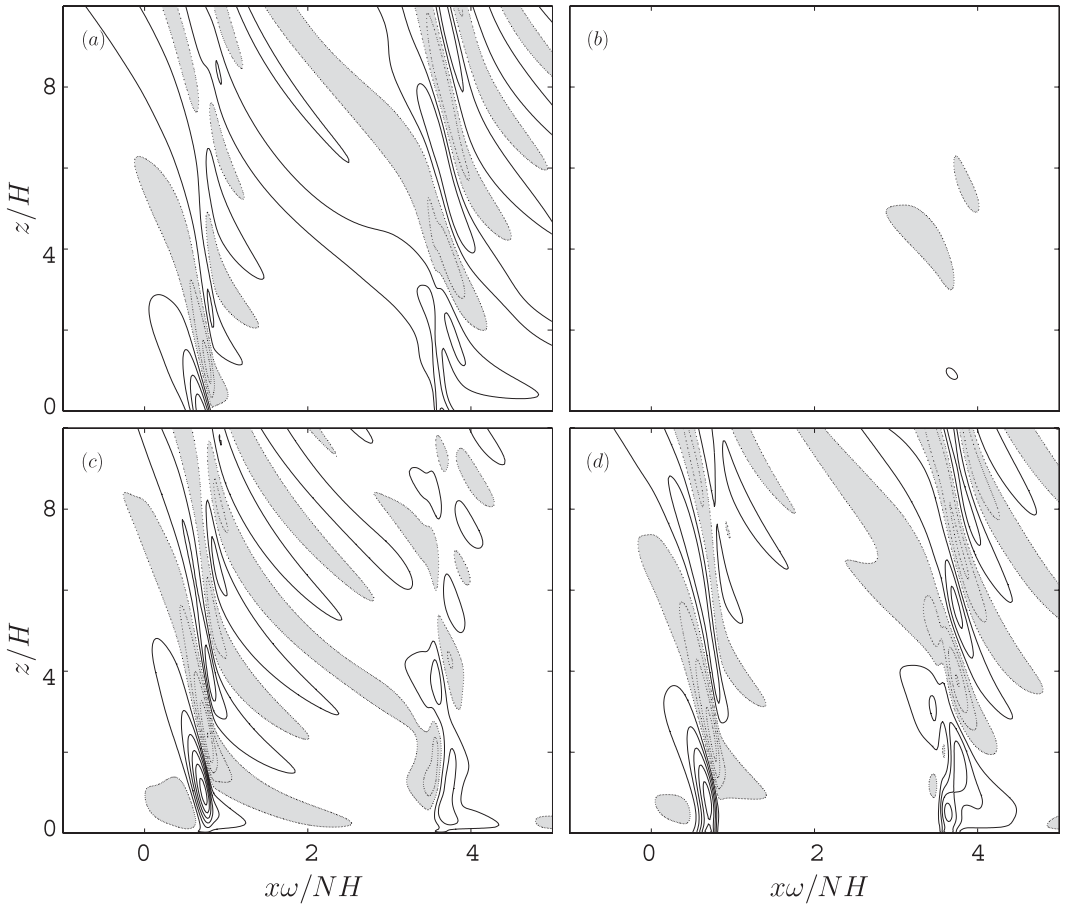

FIG. 5. The three effects of topography for the case with $\mathcal{U} = 0.625$ and $\mathcal{H} = 0.0031$ at $\omega t = \pi/2$. Vertical velocity (c.i. = 0.0024) due to (a) the disturbance flow past the plateau slope, (b) the elevated temperature gradients, and (c) the wave–wave interaction between the sea breeze and the background mountain wave. (d) The total disturbance.

larger heating amplitudes this maximum appears to trigger convective overturning.

c. Mountain-wave background state

Figure 4 shows the linear disturbance produced by the heat source for the case $\mathcal{U} = 0.625$ and with a mountain-wave background state. The corresponding disturbance for $\mathcal{H} = 0$ is shown in Figs. 2d,e.

Figures 4a and 4b show that the effect of the terrain in this case is to introduce a wave disturbance over the two slopes of the plateau. The disturbance amplitude increases with terrain height (as expected), and for a given terrain height the disturbance is significantly larger than for $\mathcal{U} = 0$ (cf. Fig. 3). Figure 4c shows the corresponding disturbance with no coastline. As before, this indicates the wave generation by the elevated heating gradients in the absence of the sea breeze. Comparing Figs. 4b and 4c suggests that the disturbance excited by the elevated heating is relatively small in this case.

As shown in the appendix, the three terrain effects outlined in section 3a can be unambiguously distinguished when the terrain height is small. Figure 5 shows the three effects in isolation for the case $\mathcal{H} = 0.0031$ and $\mathcal{U} = 0.625$, computed as given in the appendix. The fields are shown as second-order disturbances (i.e., without the leading-order sea-breeze fields). As expected from Fig. 5, the direct wave generation by elevated heating gradients in this case is relatively small (Fig. 5b). The dominant terms are then the sea-breeze flow past the plateau slopes (Fig. 5a) and the interaction of the sea breeze with the background mountain wave (Fig. 5c), which are roughly similar in size. The net disturbance is shown in Fig. 5d, showing the wave fields over the plateau slopes (cf. Fig. 4).

Finally, linear calculations with larger mountain heights suggest that the disturbance becomes unstable once the mountain height reaches some critical value (roughly for $\mathcal{H} = 0.4$). The form of the instability is similar to the instability seen in the mountain-wave problem described

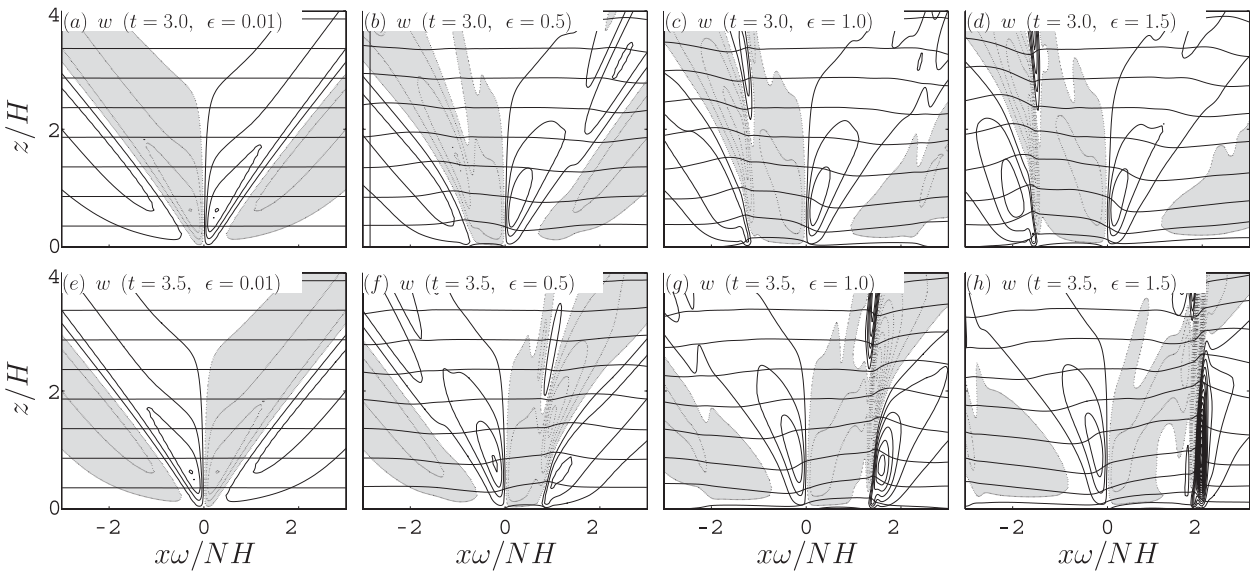

FIG. 6. The total vertical velocity (c.i. = 0.06; shaded region is negative) and isentropes (black solid line) for the $\mathcal{U} = 0, \mathcal{H} = 0$ case at (a)–(d) $t = 3.0$ days and (e),(h) $t = 3.5$ days. The heating amplitude is (a),(e) $\epsilon = 0.01$, (b),(f) $\epsilon = 0.5$, (c),(g) $\epsilon = 1.0$, and (d),(h) $\epsilon = 1.5$.

by Lee et al. (2006). This suggests that the instability is likely caused by the triad interaction.

4. Linear-to-nonlinear transition of wave response to small topography

The calculations described above give some insight into the effects of terrain on the sea breeze as considered in the linear context. However, the real problem is strongly nonlinear. In this section we consider several examples of the nonlinear behavior of the sea-breeze wave response by computing numerical simulations with varying interior heating amplitude. The emphasis is put on the transition of the system from linear to nonlinear. To keep consistent with the linear part, the results in this part are restricted to relatively small topography.

As in the previous work, we briefly check the reliability of the nonlinear model by comparing to the linear problem when the heating amplitude is very small. The comparison between Figs. 2a–c and 2d–f shows that the nonlinear model reproduces the linear results when the small heating is applied.

a. Nonlinear dynamics for $\mathcal{U} = 0$ and $\mathcal{H} = 0$

As a reference point, we begin by considering the $\mathcal{U} = 0$ case with a flat lower boundary, as described more completely by Walter (2004). Figure 6 shows the vertical velocity and potential temperature fields for the $\mathcal{H} = 0$ case for increasing values of ϵ and at two different times in the cycle: the time of maximum heating ($t = 3$ days) and the time of maximum cooling ($t = 3.5$ days).

For small ϵ, the flow fields in Fig. 6 resemble the linear inviscid solutions of QEZ10, with differences from the linear solution due entirely to viscosity (see section 2b). As ϵ increases, the fields begin to show higher-wavenumber features (Figs. 6b,f), and as ϵ approaches $\epsilon \sim 1$, these high-wavenumber features collapse to form fronts and associated density currents (Figs. 6c,g). During the maximum heating part of the cycle, the onshore propagating front is still in the early stages of forming, while the offshore-moving front from the previous cooling cycle has propagated well away from the coastline. The opposite is true at $t = 3.5$ days, when the sea-breeze front has propagated well onshore. In general, the onshore front is found to be much stronger and better defined than the leftward-moving front, and in both cases the propagation speed of the front increases with ϵ.

Figures 7a–d display the time evolution of the $\mathcal{U} = 0$, $\mathcal{H} = 0$ case for $\epsilon = 1.5$, starting at the end of the heating cycle ($t = 3.25$ days). The onshore propagating front forms late in the heating cycle (after the time of maximum heating) and continues to propagate onshore throughout the entire cooling phase (Figs. 7a–c). Toward the end of the cooling cycle the offshore front forms (Fig. 7c), and the front continues propagating offshore throughout the entire heating phase (Figs. 7a,c,d). Over time these leftward- and rightward-moving fronts dissipate as result of both viscosity and the spreading of the associated density currents.

One result of this nonlinear back-and-forth motion is that the air in the vicinity of the coastline becomes colder than it would have without the coastline [i.e., if

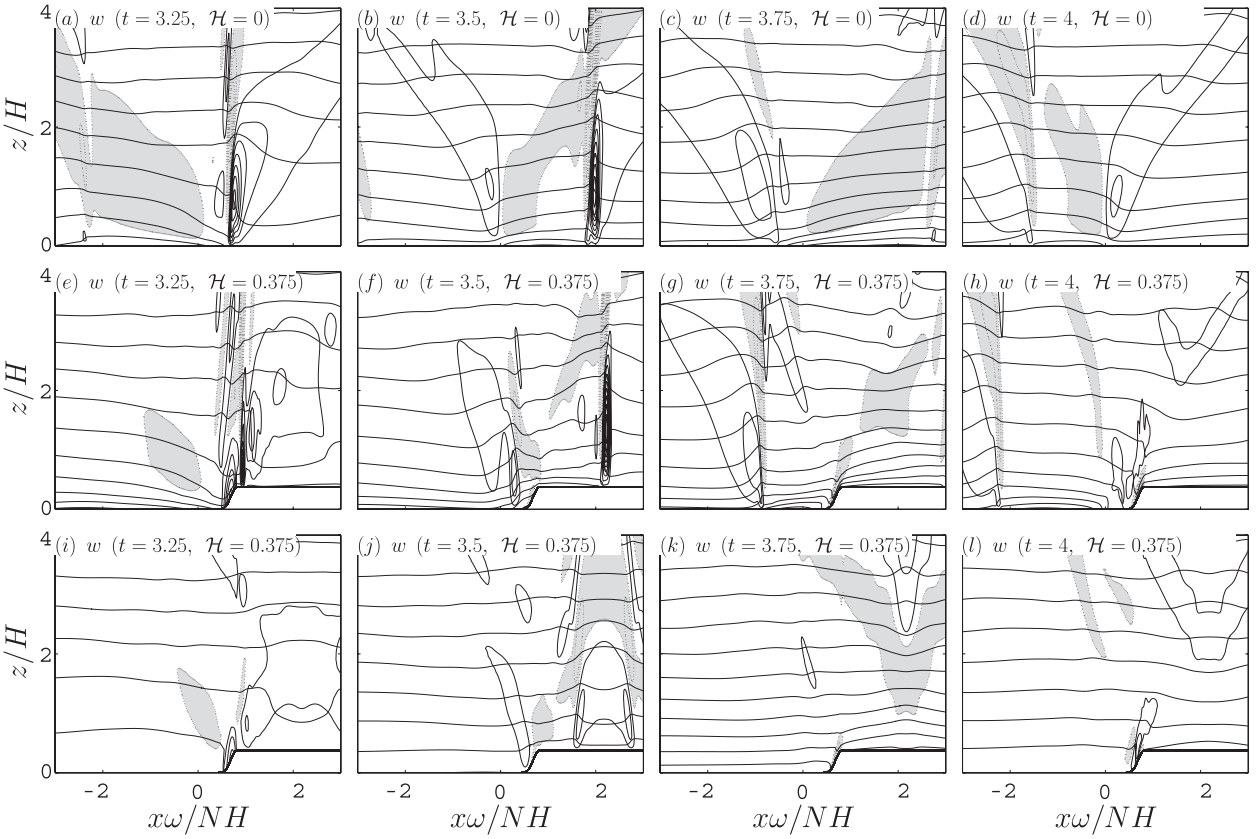

FIG. 7. (a)–(d) Time evolution of the total vertical velocity (c.i. = 0.24; shaded region is negative) and isentropes for the case $\mathcal{U} = 0$, $\mathcal{H} = 0$, and $\epsilon = 1.5$ at times $t =$ (a) 3.25, (b) 3.5, (c) 3.75, and (d) 4 days. (e)–(l) As in (a)–(d), but for (e)–(h) $\mathcal{H} = 0.375$ and (i)–(l) $\mathcal{H} = 0.375$ with no coastline.

the heat source were given by (12)]. Toward the end of the heating phase, the temperature gradient across the coastline allows the relatively colder air over the ocean to move well onshore (Figs. 7a,b). This relatively colder air then becomes even colder once the heat source switches to cooling (Figs. 7b,c). Toward the end of the cooling phase, this colder air propagates back offshore where the heating strength is much weaker, which allows the air to remain cold while the onshore air is again heated (Figs. 7c,d). The end result is a pool of colder air that propagates back and forth across the coastline.

b. *Topographic effects for $\mathcal{U} = 0$*

The effect of topography on the wave fields and fronts is illustrated in Fig. 8, which shows a series of simulations for increasing ϵ (top to bottom) and increasing values of $\mathcal{H}$ (left to right). The fields in Fig. 8 are shown at the end of the heating cycle, when the onshore front is fully formed and the leftward-moving front has propagated far from the coastline (cf. Fig. 7a).

For $\epsilon = 0.01$ and 0.25, the effects of the mountains in Fig. 8 are similar to those seen in Figs. 3a,b (note the difference in the axis scales). However, for larger ϵ the impact of the mountains is mainly to modify the fronts. For $\mathcal{H} = 0.0625$, both fronts remain essentially unchanged from the $\mathcal{H} = 0$ case (e.g., as seen in the $\epsilon = 1.0$ and 1.5 cases), but by $\mathcal{H} = 0.25$ the structure of the onshore front is strongly distorted as it climbs the plateau slope. Similarly, the offshore front propagation speed is significantly increased. For the range of $\mathcal{H}$ considered in Fig. 8, the effect of topography on the offshore propagation speed is roughly comparable to the effects of increasing ϵ (e.g., cf. Figs. 8a_4, d_4, and a_5).

Some insight into these topographic effects is provided by comparing Figs. 7e–h to Figs. 7a–d, particularly for the offshore propagating front. Shown in Figs. 7e–h is the time evolution for the $\mathcal{H} = 0.375$ case with $\epsilon = 1.5$, again starting at the end of the heating cycle. As seen in Figs. 7e,f, as the onshore moving sea-breeze front encounters the plateau, part of the low-level density current is blocked. This blocking causes cold air to be trapped at the base of the topography, where it is further cooled by the negative overnight heat source. Near the end of the cooling cycle, the cold pool is amplified further by katabatic

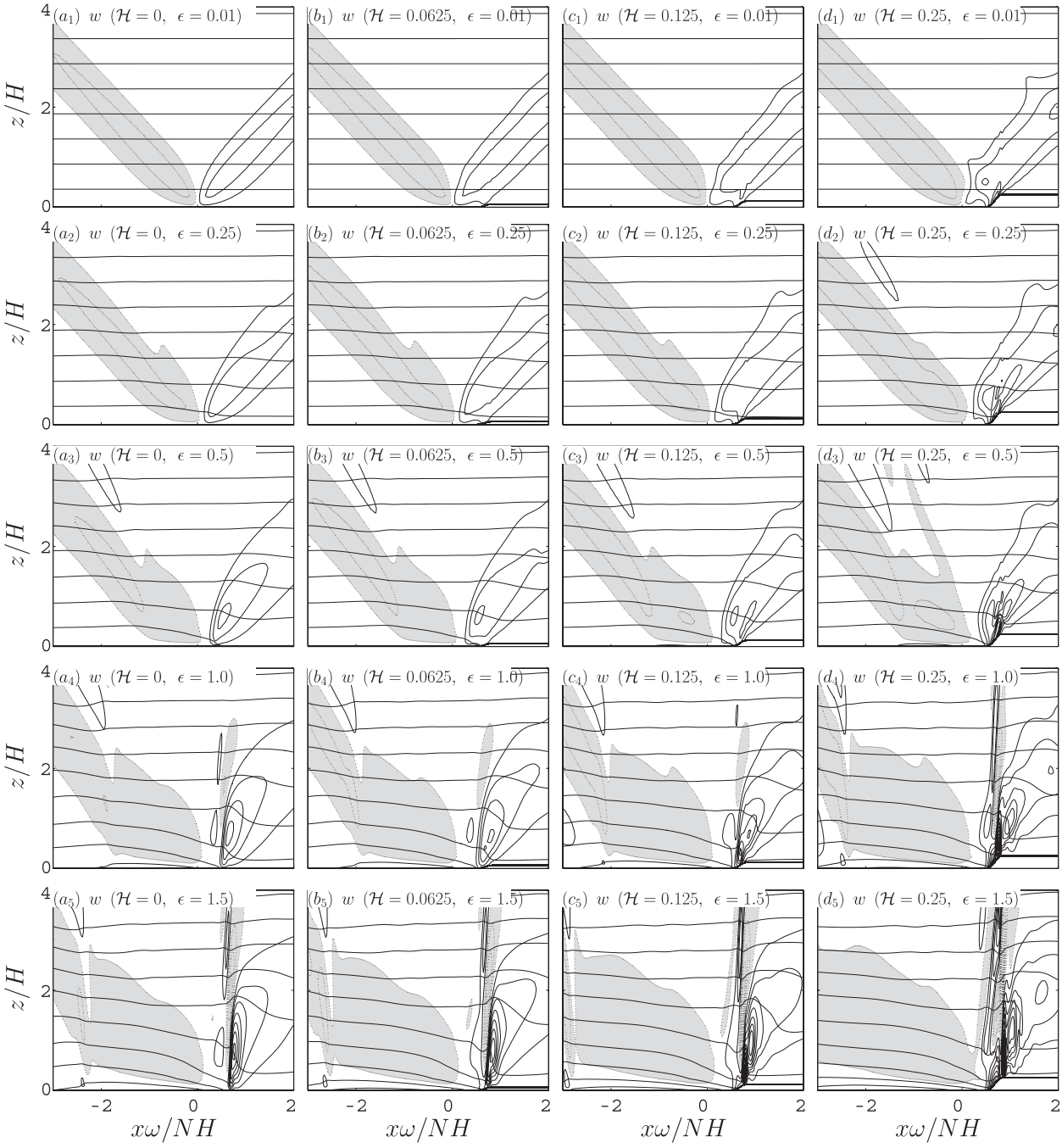

FIG. 8. (a) The total vertical velocity (c.i. = 0.12; shaded region is negative) and isentropes (black solid line) at $t = 3.25$ days with $\mathcal{U} = 0$, $\mathcal{H} = 0$, and (a_1) $\epsilon = 0.01$, (a_2) $\epsilon = 0.25$, (a_3) $\epsilon = 0.5$, (a_4) $\epsilon = 1.0$, (a_5) $\epsilon = 1.5$. (b)–(d) As in (a), but for (b) $\mathcal{H} = 0.0625$, (c) $\mathcal{H} = 0.125$, and (d) $\mathcal{H} = 0.25$.

flow down the slopes. The net result of these processes is that a significantly enhanced cold pool forms on the shoreward side of the terrain, as compared to the $\mathcal{H} = 0$ case (cf. Figs. 7f,g and 7b,c). This enhanced cold pool in turn produces a stronger density current and a more rapidly propagating offshore front (cf. Figs. 7h and 7d).

The character of the leftward-propagating front and cold pool for the cases with and without the coastal plateau is quantitatively exhibited in Fig. 9. Shown in the figure is the position of the leftward-moving front, as measured by the most negative gradient in buoyancy, as well as the center of the oscillating cold pool, as

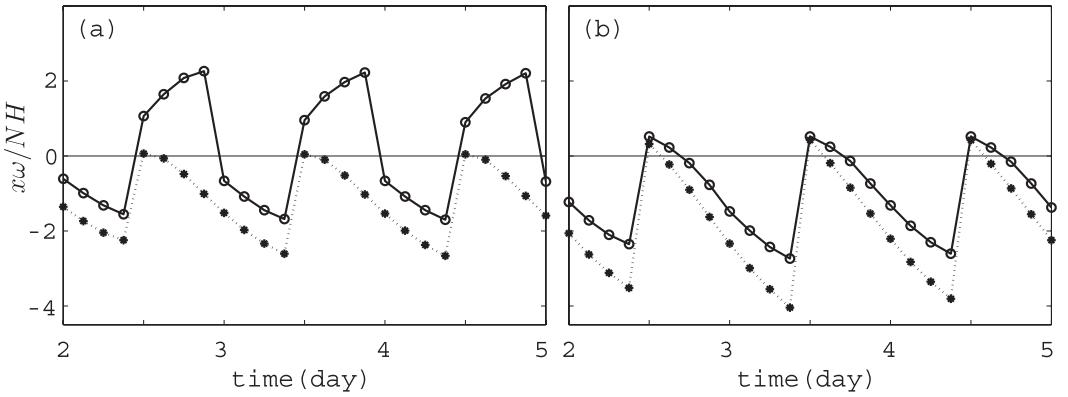

FIG. 9. Time evolution of the position of the offshore propagating front (dotted line) and the center of the cold pool (solid line) with $\mathcal{U} = 0$, $\epsilon = 1.5$, and (a) $\mathcal{H} = 0$ and (b) $\mathcal{H} = 0.375$.

measured by the most negative buoyancy at the ground. For the $\mathcal{H} = 0$ case the center of the cold pool shifts diurnally over the sea and the land. The leftward-moving front initiates along the coastline and moves toward the sea (Fig. 9a). When the terrain is added, the cold pool is mainly located over the sea and always propagates leftward, while the front initiates over the land rather than along the coastline (Fig. 9b). The shifting of the front and cold pool reflects the trapping of the sea-breeze density current as it reaches the plateau, thus preventing the cold air from extending farther inland. For reference, the characteristic dimensional value of the front speed in this case is roughly 10 m s^{-1}.

Figures 7i–l show the time evolution for the vertical velocity field with the heated topography but without the coastline [i.e., using (12) as the heat source]. The result shows that the heated topography does not introduce the propagating fronts, as seen in the cases with the coastline included. The effects of the terrain are thus not independent of the coastline: the terrain and the coastline are both needed to produce the enhanced offshore effects.

c. *Flows with background wind*

To illustrate the effects of the background wind, we again consider the case with $\mathcal{U} = 0.625$ (or dimensional wind $U = 5$ m s^{-1}). Figure 10 shows the dependence on heating amplitude and plateau height in the $\mathcal{U} = 0.625$ case, with the rows and columns arranged as in Fig. 8. The first row of the figure shows the steady-state mountain wave with no heat source (i.e., $\epsilon = 0$). The remaining rows show the disturbance from the mountain wave, as computed by subtracting the $\epsilon = 0$ case. All disturbance fields are shown at the end of the heating cycle ($t = 3.25$ days).

The first column of Fig. 10 illustrates the case with no terrain. For small ϵ, the model solutions are well described by the linear theory of QEZ10, with the main differences again due to viscosity. As ϵ increases, an onshore-propagating front becomes apparent in the w field, even though the temperature gradient is relatively weak. Comparison with the $\mathcal{U} = 0$ case (Fig. 8) shows that the propagation speed of the front is significantly increased by the effects of the wind. By contrast, the offshore propagating front in this case is completely missing. Indeed, the leftward-moving part of the disturbance remains similar to the linear solution, even for relatively large values of ϵ (at least for the time shown).

The time evolution of the $\mathcal{H} = 0$, $\mathcal{U} = 0.625$ case is shown for $\epsilon = 1.5$ in Figs. 11a–d. As shown in Fig. 11a, an onshore moving front is formed toward the end of the heating cycle, and by the time of peak cooling the front has propagated off the domain of the figure (Fig. 11b). A corresponding land-breeze front forms toward the end of the cooling cycle (Fig. 11c), but in contrast to the $\mathcal{U} = 0$ case, the front remains stationary at the coastline, disappearing by the time of peak heating. The main effect of the wind in this case is thus to enhance the onshore propagation of cold air during the warm phase but then inhibit the cold air from propagating back offshore during the cold phase. The air over the land is thus simply warmed and cooled alternately as it advects downstream with the wind.

The effects of terrain on the $\mathcal{U} = 0.625$ case are shown in the final three columns of Fig. 10. As in Fig. 8, for $\epsilon = 0.01$ the effects of the terrain are similar to those seen in the linear case (cf. Fig. 4, noting the difference in figure domains). For larger ϵ the terrain has a significant impact on both the leftward- and rightward-moving fronts. For the sea-breeze front, the main effect is to cause the front to weaken as it crosses the plateau (e.g., Figs. $10a_3$–d_3). On the other hand, the offshore front is strengthened by the terrain; unlike the $\mathcal{H} = 0$ case, for sufficiently

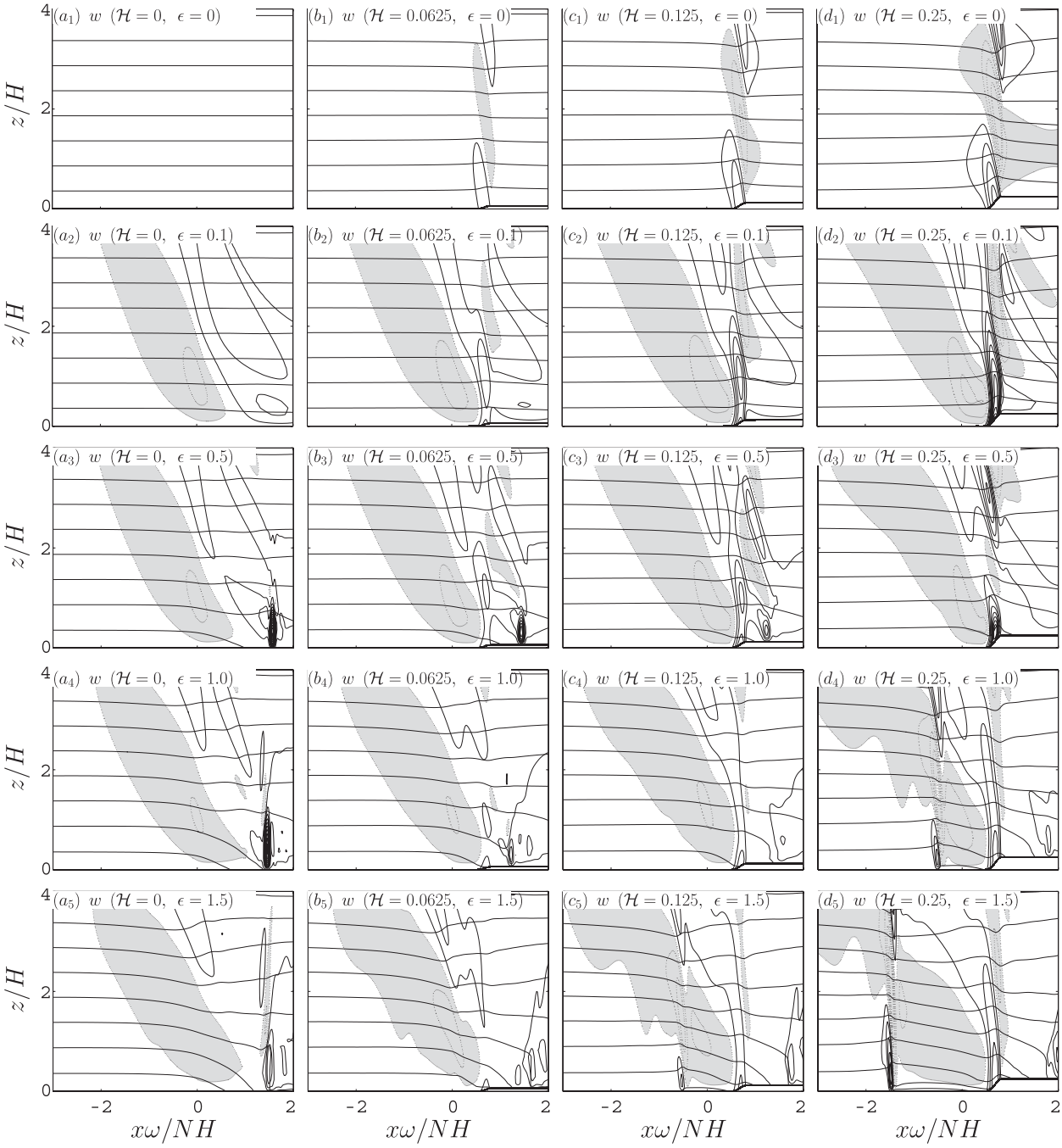

FIG. 10. (a) The vertical velocity disturbance (c.i. = 0.12; shaded region is negative) and isentropes at $t = 3.25$ days with $\mathcal{U} = 0.625$, $\mathcal{H} = 0$, and (a_1) $\epsilon = 0$, (a_2) $\epsilon = 0.1$, (a_3) $\epsilon = 0.5$, (a_4) $\epsilon = 1.0$, and (a_5) $\epsilon = 1.5$. (b)–(d) As in (a), but for (b) $\mathcal{H} = 0.0625$, (c) $\mathcal{H} = 0.125$, and (d) $\mathcal{H} = 0.25$. Except (a_1)–(d_1), all w fields are scaled as in Table 1; (a_1)–(d_1) shows the same dimensional contour interval for w as (a_5)–(d_5).

large terrain the front is able to propagate upstream (Figs. 10d_4,c_5,d_5). As in the $\mathcal{U} = 0$ case, the offshore propagation speed of the front increases with both heating amplitude and terrain height.

As illustrated by Fig. 11, the basic dynamics of these topographic effects is similar to those seen in Fig. 8. As in the $\mathcal{U} = 0$ case, the onshore moving density current becomes blocked at the base of the plateau (Figs. 11e,f), and this blocked air is cooled further once the heat source switches to cooling. By the end of the cooling phase, the air at the base of the terrain is significantly colder than in the $\mathcal{H} = 0$ case (cf. Figs. 11g and 11c).

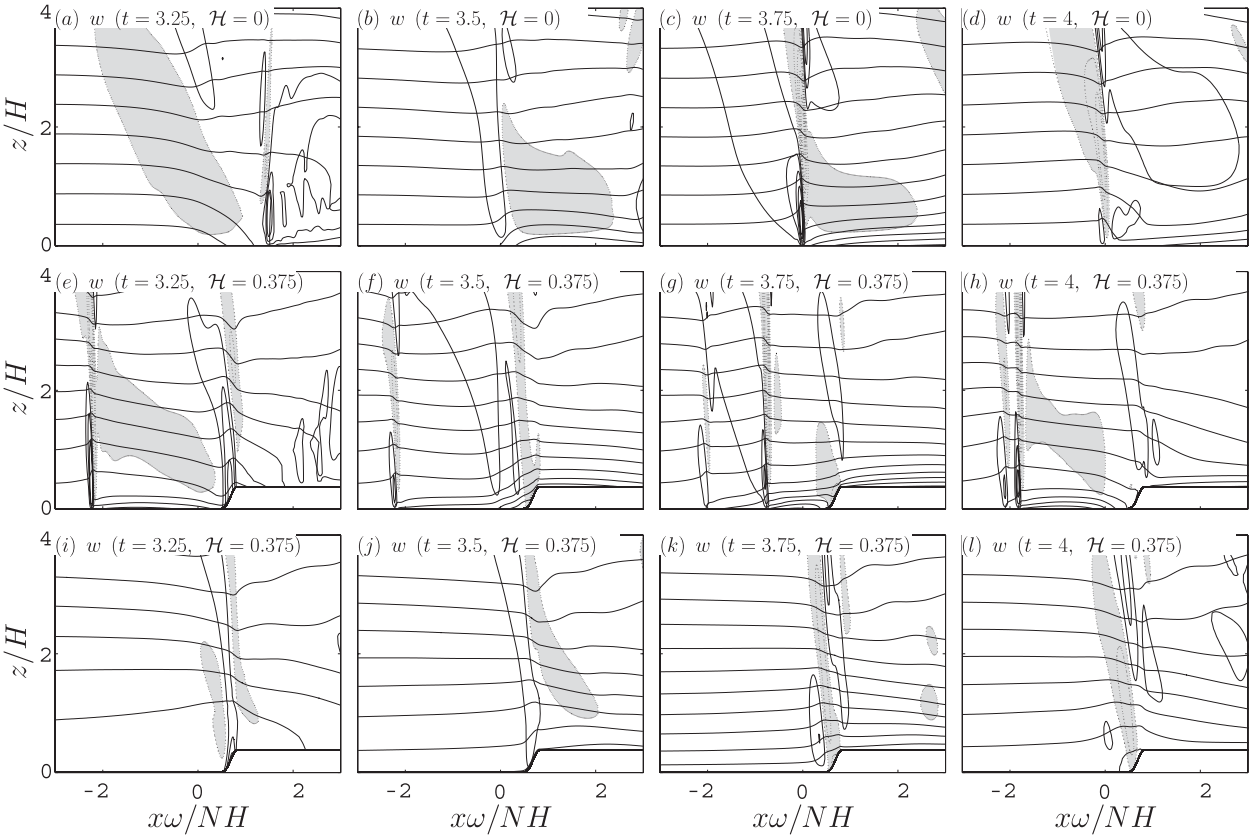

FIG. 11. (a)–(d) Time evolution of the vertical velocity disturbance (c.i. = 0.12; shaded region is negative) and isentropes (black solid line) with $\mathcal{U} = 0.625$, $\epsilon = 1.5$, and $\mathcal{H} = 0$ at $t =$ (a) 3.25, (b) 3.5, (c) 3.75, and (d) 4 days. (e)–(l) As in (a)–(d), but for (e)–(h) $\mathcal{H} = 0.375$ and (i)–(l) $\mathcal{H} = 0.375$ with no coastline.

This colder air in turn leads to a stronger density current, so that the resulting front is able to propagate upstream against the wind. Interestingly, as the density current spreads, the front slows and eventually becomes stationary (Figs. 11e,f). Each successive front then overtakes the front from the previous cycle, at times leading to a double front structure offshore (Fig. 11h).

Figure 12 illustrates the time evolution of the offshore front, the center of the cold pool, and the most negative buoyancy in the cold pool for the case with $\mathcal{U} = 0.625$, $\mathcal{H} = 0.375$, and $\epsilon = 1.5$. For most of the cycle the cold pool is centered offshore, while the front initiates near the coastline and propagates to the left. The maximum distance between the front and the coastline increases gradually with each cycle, as each front overtakes the front from the previous day (Fig. 12a). This enhanced propagation with time is due to the gradual accumulation of the cold air in the offshore cold pool, as seen in Fig. 12b. The propagation speed of the front is initially similar to the $\mathcal{U} = 0$ case but then slows as the density current spreads. As compared to the $\mathcal{U} = 0$ case, the intensity of the cold pool is stronger with $\mathcal{U} = 0.625$ (not shown), presumably due to the offshore confinement of the cold pool by the background wind.

Finally, Figs. 11i–l show the case with $\mathcal{U} = 0.625$, $\mathcal{H} = 0.375$, but without the coastal gradient in the heat source. As before, the case with no coastline produces relatively little disturbance, suggesting that the coastline and topography are both needed for the enhanced offshore cold pool.

5. Large terrain and heating depth dependence

The previous section shows the linear and nonlinear character of the coastal flow in cases with small and moderate topography. However, in many cases, the coastal terrain is larger than the case with $\mathcal{H} = 0.375$. This section will briefly explore the nonlinear phenomena under the effects of large topography. The effect of the heating depth on the circulation is also briefly considered.

a. Resting background state

The effect of larger topography on the wave fields and fronts is illustrated for the $\mathcal{U} = 0$ case in Fig. 13, which

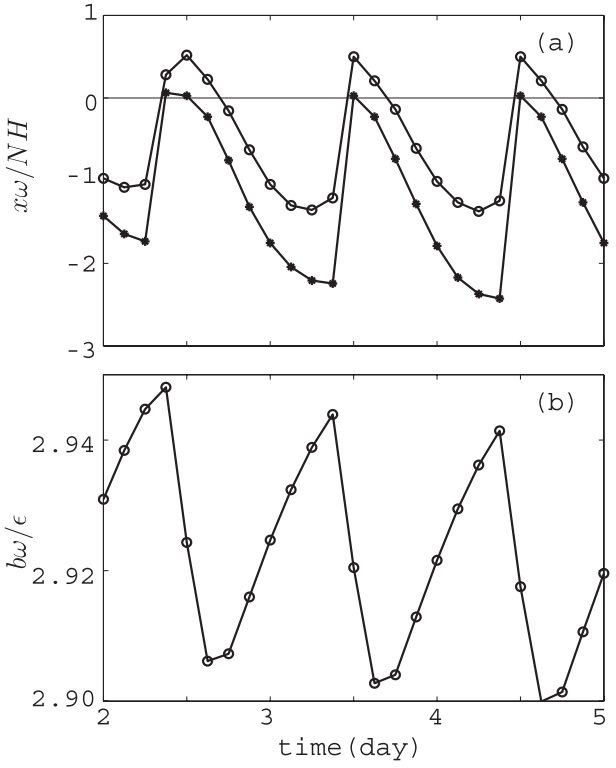

FIG. 12. Time evolution of (a) the position of the front (asterisks) and the center of the cold pool (circles), and (b) the intensity of the cold pool for the case with $\mathcal{U} = 0.625$, $\epsilon = 1.5$, $\mathcal{H} = 0.375$.

shows simulations with increasing mountain height at the end of the heating cycle.

For the flow offshore, Fig. 13 shows that there is a significant change in the speed of the land-breeze front between the smaller mountain case (Fig. 13a) and the case with $\mathcal{H} = 0.625$ (Fig. 13b). However, for larger mountain heights the increase in frontal propagation is much smaller (Figs. 13b–d). This change in the $\mathcal{H}$ dependence is presumably related to the blocking of the sea-breeze density current during the warm phase. That is, for sufficiently large $\mathcal{H}$, the density current will be blocked entirely. Further increases in $\mathcal{H}$ then lead to much smaller changes in the strength of the offshore cold pool, which in turn leads to smaller changes in the land-breeze frontal propagation. In fact, in terms of minimum buoyancy anomaly, the cold pool in actually slightly weaker at $\mathcal{H} = 2.5$ than at $\mathcal{H} = 1.25$ (at least for the time shown).

In addition to the land-breeze changes at large $\mathcal{H}$, there are also changes on the slopes of the plateau. The most notable change is a shift in the vertical velocity maximum toward the base of the plateau, along with a significant decrease in the vertical velocity magnitude at $\mathcal{H} = 2.5$. These changes in w presumably reflect the

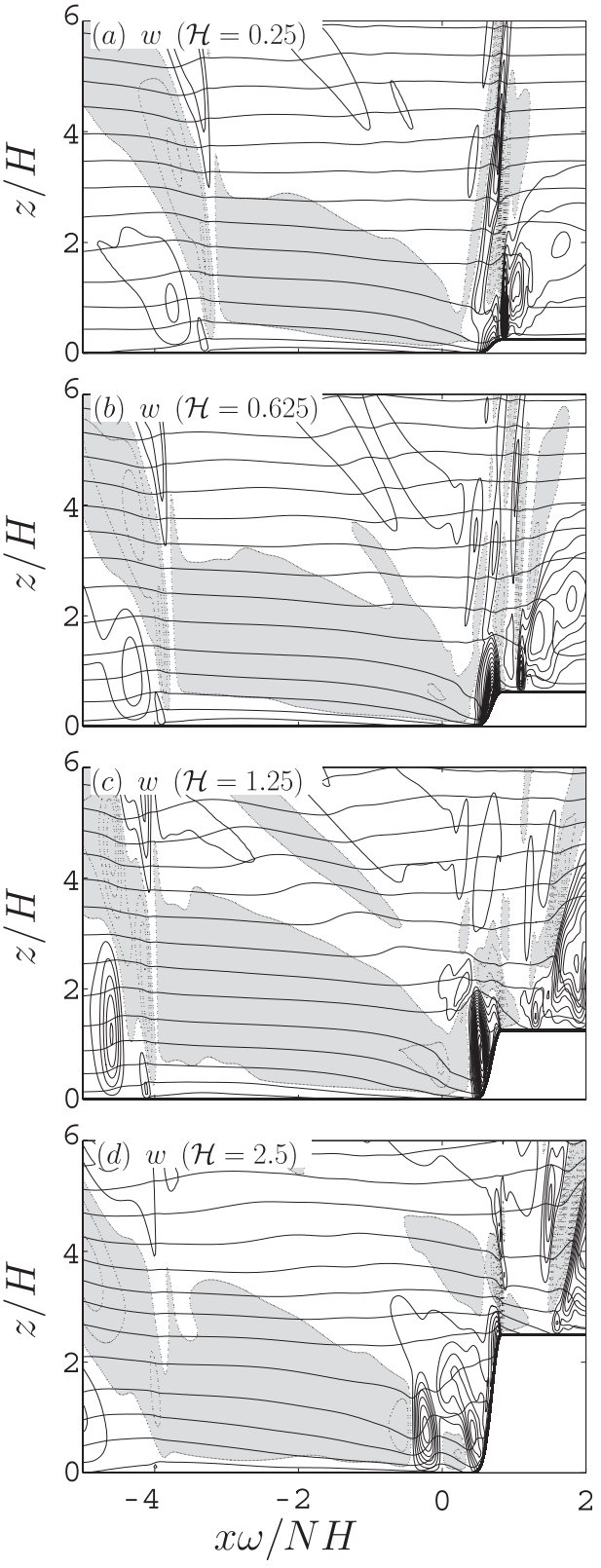

FIG. 13. Vertical velocity (c.i. = 0.12) at $t = 3.25$ days for the case with $\mathcal{U} = 0$, $\epsilon = 1.5$, and (a) $\mathcal{H} = 0.25$, (b) $\mathcal{H} = 0.625$, (c) $\mathcal{H} = 1.25$, and (d) $\mathcal{H} = 2.5$.

increase in blocking, as the low-level flow is unable to climb to the obstacle crest.

b. Flows with background wind

The effect of the background wind is illustrated in Fig. 14, which shows the $\mathcal{U} = 0.625$ case at the end of the heating cycle.

As in the $\mathcal{U} = 0$ case (shown in Fig. 13), the speed of the offshore front depends strongly on the topography height for the smaller topography cases, while for $\mathcal{H} > 0.625$ the increase with $\mathcal{H}$ is much weaker. The changes in the flow structure are also similar, as the maximum w anomaly shifts toward the base of the plateau and the minimum buoyancy in the cold pool becomes slightly less negative. Comparing Figs. 13a and 14a shows that for small terrain heights the propagation speed of the front is strongly affected by the background wind. However, for larger terrain heights the difference in propagation speeds becomes much smaller.

Figure 15 illustrates the time evolution of the flow for the case with $\mathcal{H} = 2.5$ and $\mathcal{U} = 0.625$. As in the $\mathcal{H} = 0.375$ case shown in Fig. 11e–h, the onshore flow near the end of the warm phase is blocked as the colder sea-breeze air reaches the terrain (Fig. 15a,b). However, in the $\mathcal{H} = 2.5$ case this blocking occurs through a much deeper layer, and the deeper blocked layer collapses more quickly into a land-breeze front (cf. Figs. 15b and 11f). The deeper density current in turn leads to more rapid frontal propagation, even if the minimum buoyancy at the ground is actually less negative for $\mathcal{H} = 2.5$.

c. Heating depth effect

The previous results are all obtained with the fixed heating depth ($\mathcal{H} = 800$ m). In this section, our intention is to discuss the effect of the heating depth on the wave response in a dimensional sense (i.e., varying $\mathcal{H}$ and Q_0 with the remaining dimensional parameters held fixed). Figure 16 shows the comparison of the offshore front position for the cases with topography height $h_0 = 2000$ m, $U = 0$ and 5 m s^{-1}, using different heating depths and heating amplitudes. For reference, the heating amplitude for our standard $\epsilon = 1.5$ case is $Q_0 = 8.7 \times 10^{-6}$ m s^{-3}.

With increased heating depth (at fixed Q_0), the propagation speed of the disturbance is expected to increase. However, the interpretation of this increase depends on the problem. Under linear dynamics, the effect of increased H is to produce a deeper wave response, which in turn implies faster wave propagation (in a dimensional sense). However, under nonlinear dynamics the main effect is to increase the net heating (as integrated in the vertical), which in turn produces a stronger density current.

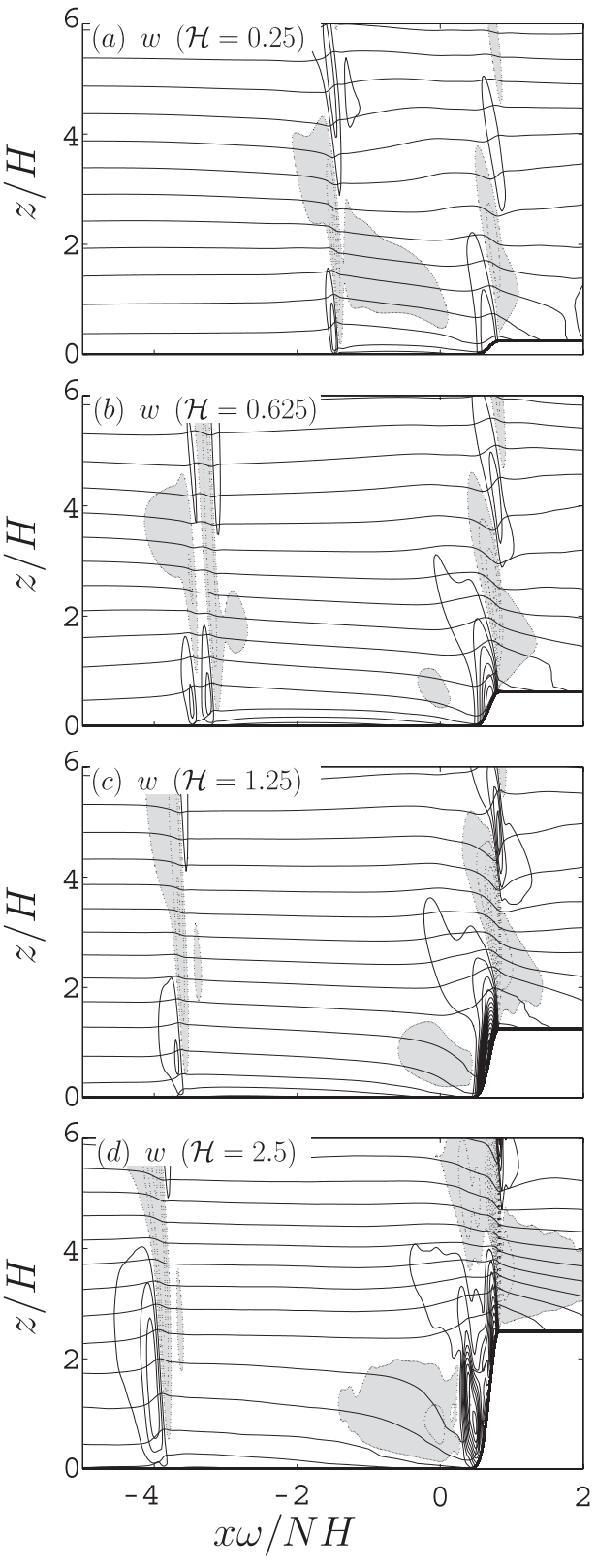

FIG. 14. Vertical velocity (c.i. = 0.24) at $t = 3.25$ days for the case with $\mathcal{U} = 0.625$, $\epsilon = 1.5$, and (a) $\mathcal{H} = 0.25$, (b) $\mathcal{H} = 0.625$, (c) $\mathcal{H} = 1.25$, and (d) $\mathcal{H} = 2.5$.

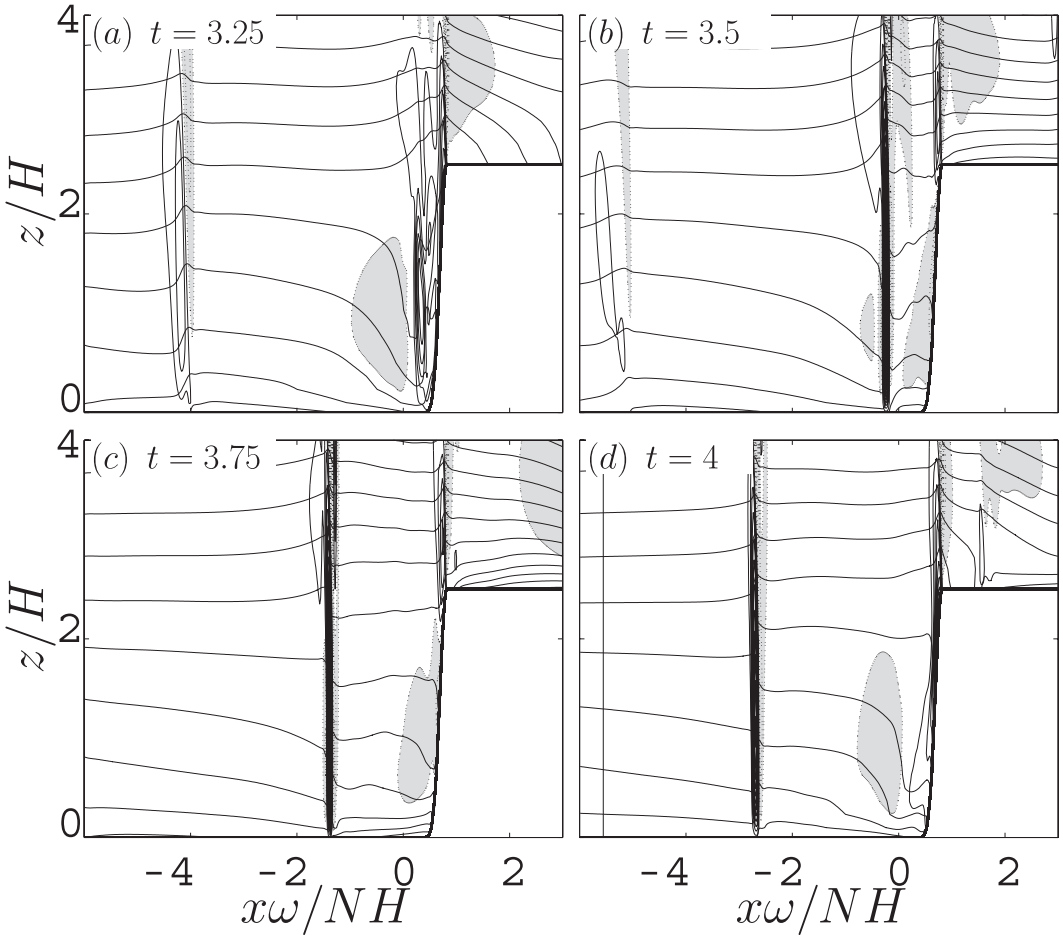

FIG. 15. Vertical velocity (c.i. = 0.36) for the case with $\mathcal{U} = 0.625$, $\epsilon = 1.5$, and $\mathcal{H} = 2.5$ at times (a) $t = 3.25$, (b) $t = 3.5$, (c) $t = 3.75$, and (d) $t = 4$ days.

As expected, in $Q_0 = 8.7 \times 10^{-6}$ m s^{-3} cases, the front for $H = 1600$ m propagates faster than the one with $H = 800$ m (Figs. 16c,e). To determine whether this increase is a linear or nonlinear effect, the front speed in the $H = 1600$ m case with $Q_0 = 4.35 \times 10^{-6}$ m s^{-3} is also calculated (Fig. 16a). In this later experiment, the vertical wavelength is still increased with the deeper heating depth, but the net integrated heating is the same as the $Q_0 = 8.7 \times 10^{-6}$ m s^{-3} case with $H = 800$ m. The result shows that the reduced heating amplitude leads to the slowest propagation of the three cases considered, showing that the dynamics of the disturbance follows the expected nonlinear trend. The $U = 5$ m s^{-1} case in Figs. 16b,d,f shows a similar result.

6. Conclusions

The equatorial sea breeze was modeled in terms of an oscillating heat source over the land. Of particular interest was the effect of an inland plateau, with the slope of the plateau located 75 km from the coastline.

Under a diurnal scale analysis, the dominant control parameters for the problem include the nondimensional heating amplitude $\epsilon = Q_0 \times (N^2 \omega H)^{-1}$, the nondimensional background wind speed $\mathcal{U} = U \times (NH)^{-1}$, and the scaled topography height $\mathcal{H} = h_0/H$. Simulations were conducted for varying values of ϵ and $\mathcal{H}$, and for $\mathcal{U} = 0$ and $\mathcal{U} = 0.625$. Both linear (or small ϵ) and nonlinear dynamics were considered, with an emphasis on moderate terrain heights ($\mathcal{H} < 1$).

In the linear problem, the sea breeze is treated as a small, diabatically forced disturbance, with either a rest state (for $\mathcal{U} = 0$) or else a steady-state mountain wave (for $\mathcal{U} = 0.625$) acting as the background flow. Compared to the $\mathcal{H} = 0$ problem of QEZ10, the linear cases with topography show additional diurnal wave disturbances over both plateau slopes, with the structure and sources of these disturbances depending on the wind

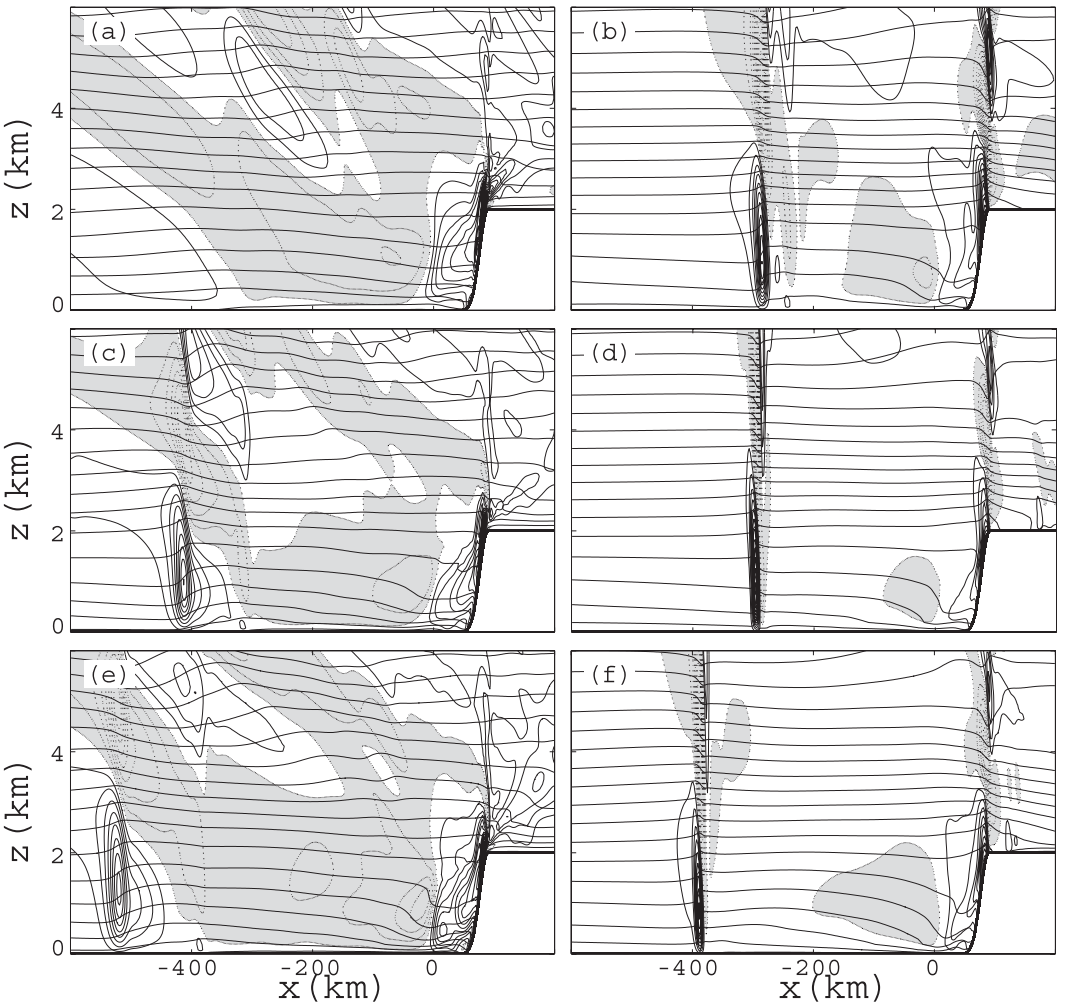

FIG. 16. Vertical velocity for $h_0 = 2000$ m and (a),(c),(e) $\mathcal{U} = 0\,\mathrm{m\,s^{-1}}$ (c.i. = 0.12) and (b),(d),(f) $\mathcal{U} = 5\,\mathrm{m\,s^{-1}}$ (c.i. = 0.36) at $t = 4$ days. The heating amplitude and heating depth are given by (a),(b) $Q_0 = 4.35 \times 10^{-6}$ m s^{-3}, $\mathcal{H} = 1600$ m; (c),(d) $Q_0 = 8.7 \times 10^{-6}$ m s^{-3}, $\mathcal{H} = 800$ m; and (e),(f) $Q_0 = 8.7 \times 10^{-6}$ m s^{-3}, $\mathcal{H} = 1600$ m.

speed. However, in no case does the linear problem produce a significant offshore effect, beyond that associated with the $\mathcal{H} = 0$ problem. Offshore effects in our experiments are thus largely nonlinear.

The transition to nonlinear effects was considered by gradually increasing ϵ, starting with the standard $\mathcal{U} = 0$ and $\mathcal{H} = 0$ problem. Nonlinearity in this problem appears first as high-wavenumber features, occurring at relatively small values of ϵ (i.e., $\epsilon \sim 0.1$). As the amplitude approaches $\epsilon \sim 1$, these nonlinear features collapse into fronts, with the propagation speed of the fronts increasing with the heating amplitude. The front for the sea breeze forms near the end of the heating cycle and propagates onshore throughout the cooling cycle, while the land-breeze front forms near the end of the cooling cycle. The sea-breeze front in this case is significantly stronger than the land-breeze front.

When terrain is added to the $\mathcal{U} = 0$ problem, the sea-breeze front becomes distorted, while the land-breeze front is significantly strengthened. For both effects, the apparent mechanism is the partial blocking of the sea-breeze density current, which traps cool air at the base of the plateau near the end of the heating cycle. This cooler blocked air is further cooled overnight, producing an enhanced cold pool on the shoreward side of the terrain, as compared to the $\mathcal{H} = 0$ case. The colder cold pool in turn leads to a stronger land-breeze density current the following morning, as well as a faster offshore propagating front. The propagation speed of the front increases with the terrain height, presumably due to increased blocking.

When an onshore wind is added (i.e., for $\mathcal{U} = 0.625$), the sea breeze propagates faster, while the land breeze is inhibited. For $\mathcal{H} = 0$, the land-breeze front remains

stationary at the coastline, even for the largest heating amplitude considered ($\epsilon = 1.5$). When the plateau is added, the land breeze again strengthens because of the same blocking and cooling mechanism as in the $\mathcal{U} = 0$ case, and for sufficiently large topography (and sufficiently large heating amplitudes) the front is able to propagate upstream. As the front propagates and spreads, it eventually becomes stationary offshore, and the front from each subsequent day then overtakes the front from the previous day.

Increasing the terrain height further (to $\mathcal{H} > 1$) leads to a number of changes in the flow, including a weakening but deepening of the land-breeze density current, as well as changes in the flow structure near the plateau peak. The mechanisms described above appear to still apply; however, the large-terrain problem was considered only briefly and likely merits further study.

It should be kept in mind that as with the previous linear studies, the current study is based on a number of simplifications and idealizations, including the use of a diurnally oscillating interior heat source. In the real problem, the heating is a complex combination of surface fluxes, turbulent mixing, and radiative effects, and the end result has both higher and lower frequencies (particularly higher harmonics) and a more complex spatial structure. The heating also has prominent day/night asymmetries. The experiments have also neglected the effects of surface friction, while at higher latitudes the Coriolis force plays a role as well. Any of these effects could potentially alter the amplitude and phasing of the flow, which could in turn modify the blocking and cooling mechanisms described above. The extent to which these complications impact real-world circulations remains a topic for future study.

Finally, it is worth noting that even with the restrictions given above, the results of this study have parallels in the problem of nocturnal coastal convection. Recent studies have revealed a tendency for nocturnal and early morning convection off coastlines, particularly in areas with near-coastal terrain. The convection starts at or near the coastline in the late evening hours and propagates offshore throughout the morning. While it remains unclear what drives these convective signals, the phasing and propagation of the signals is at least qualitatively consistent with our modeled land-breeze response, including the apparent role of topography.

Acknowledgments. This research was supported under NSF Grants ATM-0242228, ATM-0618662, ATM-0904635, ATM-1114849, and NSFC ATM-41105043; EPA Grant R03-0132; and the Basic Research Fund of the Chinese Academy of Meteorological Sciences Grant 2010Y002.

APPENDIX

Diagnostic Calculations of Terrain Effect

Consider the linearized system (7)–(12) in the limit of small terrain height h_0, and suppose the linear disturbance fields are expanded as

$$u' = u^{(0)} + u^{(1)} + \cdots, \quad w' = w^{(0)} + w^{(1)} + \cdots,$$
$$b' = b^{(0)} + b^{(1)} + \cdots, \quad P' = P^{(0)} + P^{(1)} + \cdots,$$
$$Q = Q^{(0)} + Q^{(1)} + \cdots$$

where $u^{(0)} \sim O(0)$, $u^{(1)} \sim O(h_0)$, $u^{(2)} \sim O(h_0^2)$, etc. Here, the forcing terms are derived from the Taylor series expansion of (6) as

$$Q^{(0)} = \frac{Q_0}{\pi}\left(\frac{\pi}{2} + \tan^{-1}\frac{x}{L}\right)\exp(-z/H)\cos(\omega t) \tag{A1}$$

and

$$Q^{(1)} = \frac{Q_0 h}{\pi H}\left(\frac{\pi}{2} + \tan^{-1}\frac{x}{L}\right)\exp(-z/H)\cos(\omega t). \tag{A2}$$

The background mountain wave also depends on h and is expanded as

$$u_0 = u_0^{(1)} + u_0^{(2)} + \cdots, \quad w_0 = w_0^{(1)} + w_0^{(2)} + \cdots,$$
$$b_0 = b_0^{(1)} + b_0^{(2)} + \cdots,$$

where it should be noted that the zero-order terms for the mountain wave are zero. In the present context these background terms are assumed to be known.

Then we substitute the above expressions into the basic equations (7)–(11). For small h, the zero-order system is

$$\frac{\partial u^{(0)}}{\partial t} + U\frac{\partial u^{(0)}}{\partial x} + \frac{\partial P^{(0)}}{\partial x} = 0, \tag{A3}$$

$$\frac{\partial w^{(0)}}{\partial t} + U\frac{\partial w^{(0)}}{\partial x} + \frac{\partial P^{(0)}}{\partial z} = b^{(0)}, \tag{A4}$$

$$\frac{\partial b^{(0)}}{\partial t} + U\frac{\partial b^{(0)}}{\partial x} + N^2 w^{(0)} = Q^{(0)}, \tag{A5}$$

$$\frac{\partial P^{(0)}}{\partial t} + c_s^2\left(\frac{\partial u^{(0)}}{\partial x} + \frac{\partial w^{(0)}}{\partial z}\right) = 0, \tag{A6}$$

with

$$w^{(0)}(z = 0) = 0. \tag{A7}$$

In the hydrostatic and incompressible limit, the system (A3)–(A7) with (A1) matches the $\mathcal{H} = 0$ sea-breeze problem considered by QEZ10 (as illustrated in Fig. 2). We thus refer to the zero-order solutions as the linear sea-breeze flow.

The first-order system (in h_0) is then

$$\frac{\partial u^{(1)}}{\partial t} + U\frac{\partial u^{(1)}}{\partial x} + \frac{\partial P^{(1)}}{\partial x} = -u_0^{(1)}\frac{\partial u^{(0)}}{\partial t} - w_0^{(1)}\frac{\partial u^{(0)}}{\partial z} - u^{(0)}\frac{\partial u_0^{(1)}}{\partial x} - w^{(0)}\frac{\partial u_0^{(1)}}{\partial z}, \tag{A8}$$

$$\frac{\partial w^{(1)}}{\partial t} + U\frac{\partial w^{(1)}}{\partial x} + \frac{\partial P^{(1)}}{\partial z} = -u_0^{(1)}\frac{\partial w^{(0)}}{\partial x} - w_0^{(1)}\frac{\partial w^{(0)}}{\partial z} - u^{(0)}\frac{\partial w_0^{(1)}}{\partial x} - w^{(0)}\frac{\partial u_0^{(1)}}{\partial z} + b^{(1)}, \tag{A9}$$

$$\frac{\partial b^{(1)}}{\partial t} + U\frac{\partial b^{(1)}}{\partial x} + N^2 w^{(1)} = -u_0^{(1)}\frac{\partial b^{(0)}}{\partial x} - w_0^{(1)}\frac{\partial b^{(0)}}{\partial z} - u^{(0)}\frac{\partial b_0^{(1)}}{\partial x} - w^{(0)}\frac{\partial u_0^{(1)}}{\partial z} + Q^{(1)}, \tag{A10}$$

$$\frac{\partial P^{(1)}}{\partial t} + c_s^2\left(\frac{\partial u^{(1)}}{\partial x} + \frac{\partial w^{(1)}}{\partial z}\right) = 0, \tag{A11}$$

with

$$w^{(1)} = u^{(0)}\frac{\partial h}{\partial x} - \frac{\partial w^{(0)}}{\partial z}h \quad \text{at} \quad z = 0. \tag{A12}$$

For small terrain height the system (A8)–(A12) describes the leading-order effects of the terrain. Note that since the background fields are assumed given, the right-hand side terms in (A8)–(A12) all behave as known forcing terms.

The system (A8)–(A12) shows that at leading order, the three terrain effects mentioned in section 3a can be cleanly separated: (i) the elevated heating gradients are described by the $Q^{(1)}$ term in (A10), (ii) the sea-breeze flow past the terrain slopes is described by (A12), and (iii) the interaction between the sea breeze and the background mountain wave is described by the advection terms on the right in (A8)–(A10). Since the system is linear, the response to these three forcing terms can be computed independently.

Solutions to (A8)–(A12) are computed using a modified version of the linear model described in section 3a. The model solves (7)–(10), but with the lower boundary condition specified as

$$w' = -\frac{\partial w'}{\partial z}h + u'\frac{\partial h}{\partial x} \quad \text{at} \quad z = 0$$

and with Q set equal to $Q^{(0)} + Q^{(1)}$. The terrain height is set to a small but nonzero value. To within $O(h_0^2)$ corrections, the resulting model fields can then be interpreted as $u^{(0)} + u^{(1)}$, $w^{(0)} + w^{(1)}$, etc.

A companion model run with $h_0 = 0$ gives the zero-order fields, and subtracting the two runs leaves the first-order corrections $u^{(1)}$, $w^{(1)}$, etc. Contributions from the individual forcing terms are then computed by including only the associated terms in the solution to (7)–(10), with the other forcing terms set explicitly to zero.

REFERENCES

Antonelli, M., and R. Rotunno, 2007: Large-eddy simulation of the onset of the sea breeze. *J. Atmos. Sci.,* **64,** 4445–4457.

Carbone, E. R., J. D. Tuttle, D. A. Ahijevych, and S. B. Trier, 2002: Inferences of predictability associated with warm season precipitation episodes. *J. Atmos. Sci.,* **59,** 2033–2056.

Cenedese, A., M. Miozzi, and P. Monti, 2000: A laboratory investigation of land and sea breeze regimes. *Exp. Fluids,* **29,** 291–299.

Crosman, E. T., and J. D. Horel, 2010: Sea and lake breezes: A review of numerical studies. *Bound.-Layer Meteor.,* **137,** 1–29.

Dalu, G. A., and R. A. Pielke, 1989: An analytical study of the sea breeze. *J. Atmos. Sci.,* **46,** 1815–1825.

Davis, W. M., G. Schultz, and R. D. Ward, 1889: An investigation of the sea-breeze. *New Engl. Meteor. Soc. Obser.,* **21,** 214–264.

Defant, F., 1951: *Compendium of Meteorology*. American Meteorological Society, 1334 pp.

Drobinski, P., and T. Dubos, 2009: Linear breeze scaling: From large-scale land/sea breezes to mesoscale inland breezes. *Quart. J. Roy. Meteor. Soc.,* **135,** 1766–1775.

Epifanio, C. C., 2007: A method for imposing surface stress and heat flux conditions in finite-different models with steep terrain. *Mon. Wea. Rev.,* **135,** 906–917.

——, and T. Qian, 2008: Wave–turbulence interactions in a breaking mountain wave. *J. Atmos. Sci.,* **65,** 3139–3158.

Estoque, M. A., 1961: A theoretical investigation of the sea breeze. *Quart. J. Roy. Meteor. Soc.,* **87,** 136–136.

Finkele, K., J. M. Hacker, H. Kraus, and R. A. Byron-Scott, 1995: A complete sea-breeze circulation cell derived from aircraft observations. *Bound.-Layer Meteor.,* **73,** 299–317.

Fisher, E. L., 1960: An observational study of the sea breeze. *J. Meteor.,* **17,** 645–660.

——, 1961: A theoretical study of the sea breeze. *J. Meteor.,* **18,** 216–233.

Fovell, R. G., 2005: Convective initiation ahead of the sea-breeze front. *Mon. Wea. Rev.,* **133,** 264–278.

Gal-Chen, T., and R. C. J. Somerville, 1975: Numerical solution of the Navier-Stokes equations with topography. *J. Comput. Phys.,* **17,** 276–310.

Hara, T., Y. Ohya, T. Uchida, and R. Ohba, 2009: Wind-tunnel and numerical simulations of the coastal thermal internal boundary layer. *Bound.-Layer Meteor.,* **130,** 365–381.

Haurwitz, B., 1947: Comments on the sea-breeze circulation. *J. Meteor.,* **4,** 1–8.

He, H., and F. Zhang, 2010: Diurnal variations of warm-season precipitation over North China. *Mon. Wea. Rev.,* **138,** 1017–1025.

Imaoka, K., and R. W. Spencer, 2000: Diurnal variation of precipitation over the tropical oceans observed by TRMM/TMI combined with SSM/I. *J. Climate,* **13,** 4149–4158.

Jeffreys, H., 1922: On the dynamics of wind. *Quart. J. Roy. Meteor. Soc.,* **48,** 29–46.

Klemp, J. B., and R. B. Wilhelmson, 1978: The simulation of three-dimensional convective storm dynamics. *J. Atmos. Sci.,* **35,** 1070–1096.

Koch, S. E., F. Zhang, M. L. Kaplan, Y.-L. Lin, R. Weglarz, and C. M. Trexler, 2001: Numerical simulations of a gravity wave event over CCOPE. Part III: The role of a mountain–plains solenoid in the generation of the second wave episode. *Mon. Wea. Rev.,* **129,** 909–932.

Lee, Y., D. J. Muraki, and D. E. Alexander, 2006: A resonant instability of steady mountain waves. *J. Fluid Mech.,* **568,** 303–327.

Lilly, D. K., 1962: On the numerical simulation of buoyant convection. *Tellus,* **14,** 148–172.

Mapes, B. E., T. T. Warner, M. Xu, and A. J. Negri, 2003a: Diurnal patterns of rainfall in northwestern South America. Part I: Observations and context. *Mon. Wea. Rev.,* **131,** 799–812.

——, ——, and —— , 2003b: Diurnal patterns of rainfall in northwestern South America. Part III: Diurnal gravity waves and nocturnal convection offshore. *Mon. Wea. Rev.,* **131,** 830–844.

Miller, S. T. K., B. D. Keim, R. W. Talbot, and H. Mao, 2003: Sea breeze: Structure, forecasting, and impacts. *Rev. Geophys.,* **41,** 1011, doi:10.1029/2003RG000124.

Pearce, R. P., 1955: The calculation of a sea-breeze circulation in terms of the differential heating across the coastline. *Quart. J. Roy. Meteor. Soc.,* **81,** 351–381.

——, R. C. Smith, and J. S. Malkus, 1956: Discussion of ''The calculation of a sea-breeze circulation in terms of the differential heating across the coast line,'' ''Theory of air over a heated land mass,'' and ''The effects of a large island upon the trade-wind air stream.'' *Quart. J. Roy. Meteor. Soc.,* **82,** 235–241, doi:10.1002/qj.49708235211.

Pierson, W. J., 1950: The effects of eddy viscosity, Coriolis deflection, and temperature fluctuation on the sea breeze as a function of time and height. *Meteorological Papers,* Vol. 1, College of Engineering, New York University, 30 pp.

Puygrenier, V., F. Lohou, B. Campistron, F. Saïd, G. Pigeon, B. Bénech, and D. Serça, 2005: Investigation on the fine structure of sea-breeze during ESCOMPTE experiment. *Atmos. Res.,* **74,** 329–353.

Qian, T., C. Epifanio, and F. Zhang, 2010: Linear theory calculations for the sea breeze in a background wind: The equatorial case. *J. Atmos. Sci.,* **66,** 1749–1763.

Rotunno, R., 1983: On the linear theory of the land and sea breeze. *J. Atmos. Sci.,* **40,** 1999–2009.

Schmidt, F. H., 1947: An elementary theory of the land- and sea-breeze circulation. *J. Meteor.,* **4,** 9–20.

Simpson, J. E., 1997: *Gravity Currents in the Environment and the Laboratory*. Vol. 4. Cambridge University Press, 244 pp.

Walsh, J. E., 1974: Sea breeze theory and applications. *J. Atmos. Sci.,* **31,** 2012–2026.

Walter, K. R., 2004: The nonlinear dynamics of the sea breeze. M.S. thesis, Texas A&M University, 112 pp.

Warner, T. T., B. E. Mapes, and M. Xu, 2003: Diurnal patterns of rainfall in northwestern South America. Part II: Model simulation. *Mon. Wea. Rev.,* **131,** 813–829.

Yang, G., and J. Slingo, 2001: The diurnal cycle in the tropics. *Mon. Wea. Rev.,* **129,** 784–801.

Zhang, F., and S. E. Koch, 2000: Numerical simulation of a gravity wave event over CCOPE. Part II: Waves generated by an orographic density current. *Mon. Wea. Rev.,* **128,** 2777–2796.

Zhang, Y., Y. Chen, T. Schroeder, and K. Kodama, 2005: Numerical simulations of sea-breeze circulations over northwest Hawaii. *Wea. Forecasting,* **20,** 827–846.